

# Data report: minor element concentrations in pore fluids from the CRISP-A transect drilled during Expedition 334<sup>1</sup>

Marta E. Torres,<sup>2</sup> Jesse M. Muratli,<sup>2</sup> and Evan A. Solomon<sup>3</sup>

## Chapter contents

<a href="#">Abstract</a> .....	1
<a href="#">Introduction</a> .....	1
<a href="#">Study sites</a> .....	2
<a href="#">Analytical methods</a> .....	3
<a href="#">Results and discussion</a> .....	4
<a href="#">Acknowledgments</a> .....	5
<a href="#">References</a> .....	6
<a href="#">Figures</a> .....	8
<a href="#">Tables</a> .....	12

## Abstract

We report on the minor element composition of pore fluids recovered during Integrated Ocean Drilling Program (IODP) Costa Rica Seismogenesis Project (CRISP) Expedition 334 from two sites (U1378 and U1379) drilled in the slope sediments of the overriding Caribbean plate and one site (U1381) that sampled sediments in the incoming Cocos plate. Sr, Ba, Li, B, and Mn were measured using a Leeman Labs Prodigy inductively coupled plasma–optical emission spectrometry, on acidified dilutions of pore water samples at Oregon State University.  $H_4SiO_4$  concentrations were determined colorimetrically in unacidified samples using a Thermo Scientific Genesys 10s Vis spectrophotometer at the University of Washington.

In the slope sediment, alteration of reactive ash layers exerts a control on  $H_4SiO_4$  concentrations and leads to increases in Ba and to some degree Mn. Sr is also released from this reaction, but the pore water profiles also reflect carbonate diagenesis, which is also known to occur in these sediments. Li increases with depth and has a discrete maximum at a shear zone that marks the unconformity between the slope apron sediments and the underlying margin wedge. B shows an increase over seawater values in the shallowest sediments, possibly due to release of this element from organic matter alteration. A decrease below the near-surface maxima suggests incorporation of this element on clay minerals.

At the incoming site, the concentration-depth profile of  $H_4SiO_4$  reflects lithology with lower concentrations in Unit I and elevated concentrations in Unit II resulting from biogenic silica dissolution. Sr reflects ash alteration within the sediments, and a reversal close to the sediment basement contact indicates diffusional communication with altered seawater in the oceanic basement. Li and Mn profiles are also indicative of diffusional communication with the basement aquifer.

## Introduction

The Costa Rica Seismogenesis Project (CRISP) was designed to understand the processes that control fault zone behavior during earthquake nucleation and rupture propagation at erosional subduction zones. The CRISP study area, located offshore the Osa Peninsula of Costa Rica, is part of the active and long-lived subduction erosion from Guatemala to Costa Rica (Ranero et al.,

<sup>1</sup>Torres, M.E., Muratli, J.M., and Solomon, E.A., 2014. Data report: minor element concentrations in pore fluids from the CRISP-A transect drilled during Expedition 334. In Vannucchi, P., Ujiie, K., Stroncik, N., Malinverno, A., and the Expedition 334 Scientists, *Proc. IODP, 334*: Tokyo (Integrated Ocean Drilling Program Management International, Inc.).

doi:10.2204/iodp.proc.334.201.2014

<sup>2</sup>College of Earth, Ocean, and Atmospheric Science, 104 CEOAS Administration Building, Oregon State University, Corvallis OR 97331, USA. Correspondence author:

[mtorres@coas.oregonstate.edu](mailto:mtorres@coas.oregonstate.edu)

<sup>3</sup>School of Oceanography, University of Washington, Seattle WA 98195, USA.



2000; Ranero and von Huene, 2000; Vannucchi et al., 2004). This area is characterized by low sediment supply, fast convergence rate, abundant plate interface seismicity, and a change in subducting plate relief along strike (see the “[Expedition 334 summary](#)” chapter [Expedition 334 Scientists, 2012a]). Arcward of the trench, the lower slope consists of a 10–12 km wide frontal prism where a modern sediment apron overlies older sediments that may have been deposited on an older fore-arc basin setting. The first phase of this project focuses on sampling of sediments, fluids, and crustal rocks to fully characterize the eroding material before subduction.

A fundamental component of our understanding of the subduction input focuses on sampling sediments, fluids, and crustal rocks because fluids and associated diagenetic reactions affect hydrological parameters (e.g., permeability and pore pressure) and may regulate the mechanical state of the plate interface at depth. Because of time constraints imposed by a short expedition with high recovery and the importance of fully constraining the fluid regime during Integrated Ocean Drilling Program (IODP) Expedition 334, we concentrated our efforts on collecting samples for postcruise studies, and only a limited number of analyses was carried out onboard. Here we report on the concentration of minor elements of samples collected from coring at two slope sites (Site U1378 on the middle slope and Site U1379 on the upper slope) and at one site on the Cocos plate (Site U1381) (Fig. [F1](#)). These data were used to complement geochemical interpretations based on shipboard results from a second IODP expedition (344) to this margin in 2012 (Harris, Sakaguchi, Petronotis, and the Expedition 344 Scientists, 2013) and strontium isotopic analyses of fluids collected during both Expeditions 334 and 344 (Ross et al., submitted).

## Study sites

The main aim of Expedition 334 was to characterize the sediments in the upper (Site U1379) and middle (Site U1378) slope of the Caribbean plate and the incoming sediment and igneous crust of the Cocos plate (Site U1381). Complete descriptions of the drilling results are in each site chapter of this volume.

### Site U1378

Site U1378 is located above the unlocked portion of the plate boundary, as indicated by interplate earthquake relocation and geodetic measurements

(LaFemina et al., 2009). The margin here consists of an upper plate framework wedge underlying about 564 m of slope sediments. Drilling at this site penetrated a landward dipping reflector interpreted as a normal fault cutting through the whole upper plate, which may be directly linked with the plate boundary fluid system. Site U1378 is dominantly composed of a monotonous sequence of silty clay to clay that alternates with widely interspersed centimeter-scale sandy layers, which was divided into two main lithostratigraphic units (Fig. [F2](#)). Unit I (~128 m thick) is composed of mainly soft, dark greenish gray terrigenous silty clay. Unit II (~386 m thick) consists predominantly of massive, well consolidated, olive-green terrigenous clayey silt(stone) and silty clay(stone). Shipboard sedimentologists identified 82 tephra layers, which seem to be quite heterogeneous in composition. The lowermost core recovered from Hole U1378B (Core 334-U1378B-63X) contains a 0.97 m thick sequence of extensively fractured silty claystones.

### Site U1379

The shallowest site along the CRISP transect, Site U1379 is thought to overly the locked portion of the subduction zone seismogenic zone in an area where the plate boundary is 4.5 km below seafloor. The sediments are predominantly a monotonous sequence of silty clay to clay that alternates with widely interspersed decimeter-scale sandy layers. Sediments from Site U1379 are divided into five lithostratigraphic units. Unit I, the relatively thin top unit, consists of medium- to coarse-grained sand with abundant shell fragments. Unit II (~650 m thick) is composed of mainly olive-green clayey silt(stone) and silty clay(stone) with minor layers of tephra. The sediments in this unit are massive and well consolidated; the tephra layers are unlithified. Hardened concretions of carbonate mud are present in the interval between Cores 334-U1379C-16H and 40X (~79–305 meters below seafloor [mbsf]). Unit III (~229 m thick) consists of fining- and coarsening-upward sequences (decimeter thick) of olive-green silty sands and sandstone. Tephra layers are sparse in this unit, accumulating mainly in one sequence within the upper part of the unit. Unit IV (~2 m thick) consists of carbonate-cemented medium- to coarse-grained sand with well-rounded, lithic pebble-sized clasts and thick-walled shell shards. Unit V (~67 m thick) is composed of matrix-supported breccia with clasts of limestone, basalt, and mudstone in a fine sandy matrix intercalated. Pore waters were sampled only from sediments recovered from lithostratigraphic Units I to III (Fig. [F3](#)). Overall, 53 tephra layers (2–45

cm thick) were identified intercalated in the background sedimentation of the different units, the majority of them below 324 mbsf.

### Site U1381

Site U1381 targeted the sediment and basement sequences in the incoming Cocos plate. The upper 50 mbsf of sediment at this site is composed of a predominantly monotonous sequence of silty clay to clay (Unit I); which is underlayed by a more pelagic sequence (Unit II), characterized by abundant biogenic components (Fig. F4). The contact between the basement and the overlying sediment was recovered at ~95 mbsf.

## Analytical methods

Pore fluids were collected from whole-round cores that were cut on the catwalk immediately after recovery, capped, and taken to the laboratory for processing using a titanium squeezer, modified after the stainless-steel squeezer of Manheim and Sayles (1974). Gauge pressures up to 30 MPa were applied using a laboratory hydraulic press to extract pore water. Interstitial water was passed through a pre-washed Whatman No. 1 filter fitted above a titanium screen, filtered through a 0.2  $\mu\text{m}$  Gelman polysulfone disposable filter, and subsequently extruded into a pre-cleaned (10% HCl) 60 mL plastic syringe attached to the bottom of the squeezer assembly. Details of the procedure are given in the “Methods” chapter (Expedition 334 Scientists, 2012b).

For the minor element concentration analyses (B, Ba, Fe, Li, Mn, and Sr), the interstitial water sample aliquot was diluted by a factor of 10 (54 of the Hole U1379C samples; 0.25 mL sample added to 2.25 mL 1% nitric acid) or 15 (all other samples; 0.2 mL sample added to 2.8 mL 1% nitric acid). Only B, Ba, and Li data were collected from the 54 Hole U1379C samples that were diluted 10-fold; and these samples were further diluted 20-fold (0.2 mL diluted sample added to 3.8 mL 1% nitric acid, for a total dilution factor of 200) before acquiring Sr data. Iron and Mn data were not acquired for these samples. Because of the high concentration of matrix salts in the interstitial water samples at the 10- and 15-fold run dilutions, matrix matching of the calibration standards was necessary to achieve accurate results by inductively coupled plasma–optical emission spectrometry. To this end, a matrix solution was prepared from trace-metal-pure salts (NaCl, CaCl<sub>2</sub>, and MgSO<sub>4</sub>; Sigma Aldrich, USA). These ultrapure salts contributed a not insignificant amount of Ba to the solution, determined to be ~13 nM. This contribution

was accounted for when we determined the Ba concentrations in the calibration standards.

The calibration standards used for acquiring B, Ba, and Li data from the 10-fold diluted samples were made in 1% nitric acid from 1000  $\mu\text{g}/\text{mL}$  primary standards (Ultra Scientific, USA) and matrix-matched using our matrix solution. Calibration standard dilutions were done by weight, allowing for a concentration to be calculated in each solution. Standards ranged from 0.178 to 18.2  $\mu\text{M}$  Li, 11.3 to 1155  $\mu\text{M}$  B, and 10.3 to 917 nM Ba (accounting for Ba contributed from the matrix solution). Calibration standards used to calculate Sr in these samples were diluted by weight with 1% nitric acid from an in-house stock solution containing 1  $\mu\text{g}/\text{mL}$  Sr. These standards were not matrix-matched to the samples, as we assumed the 200-fold dilution would dilute the sample matrix sufficiently. The standards ranged from 0.0441 to 2.04  $\mu\text{M}$  Sr.

The stock standard solution used while running all other samples was prepared from 1000  $\mu\text{g}/\text{mL}$  primary standards (Ultra Scientific and BDH Chemical) in a 1% nitric acid solution. This solution contained the following concentrations of elements: B = 108.0  $\mu\text{M}$ , Ba = 1.233  $\mu\text{M}$ , Fe = 5.381  $\mu\text{M}$ , Li = 43.99  $\mu\text{M}$ , Mn = 5.571  $\mu\text{M}$ , and Sr = 27.42  $\mu\text{M}$ . This standard solution was diluted by weight with 1% nitric acid, with dilution factors of 3, 10, 30, 100, and 300, and each dilution was matrix-matched using our matrix solution.

Calibration standards were run multiple times each run day, and the sample concentrations were calculated using a regression of all calibration data points. The daily limit of detection was determined through error analysis of these regressions. The error due to the regression was calculated for each individual standard run, and a second-order polynomial was fit to these error values. The limits of detection reported here are from the point at which the concentration is equal to three times its corresponding error value along this curve. Because this limit was calculated each day, it is variable between runs. Detection limits, corrected for sample dilution, range from 4.3 to 6.4  $\mu\text{M}$  B, 70 to 84 nM Ba, 0.25 to 0.34  $\mu\text{M}$  Fe, 0.82 to 2.4  $\mu\text{M}$  Li, 0.19 to 0.28  $\mu\text{M}$  Mn, and 0.67 to 1.1  $\mu\text{M}$  Sr.

Accuracy and precision of the samples were estimated by repeated analysis of IAPSO standard seawater (Ocean Scientific International Ltd., United Kingdom), with a salinity of 34.993. Values with 2 $\sigma$  errors ( $n = 26$ ) were B =  $452 \pm 14$   $\mu\text{M}$ , Ba =  $631 \pm 31$  nM, Li =  $25.8 \pm 0.9$   $\mu\text{M}$ , and Sr =  $88.0 \pm 1.3$   $\mu\text{M}$ . Iron and Mn were always below the detection limit for each day’s run. For these elements the average ana-

lytical precision was estimated from the repeated runs of the standard curves, and was <5% for Fe and ≤2% for Mn.

Dissolved silica concentrations were determined on shore with a Thermo Scientific Genesys 10s Vis spectrophotometer at the University of Washington using the colorimetric method described in Gieskes et al. (1991). Briefly, the method is based on the production of a yellow silicomolybdate complex and the subsequent reduction of this complex to yield a blue color. Standards and samples were prepared for analysis by diluting 20 times then adding the molybdate solution to the vials. Approximately 15 min was allowed for complexation with the molybdate solution before reduction with a solution consisting of metol sulfite, oxalic acid, and sulfuric acid. After addition of the reducing solution, the samples were allowed to sit for at least 3 h to let the blue color develop before the absorbance was read on the spectrophotometer at a wavelength of 812 nm.

Calibration, check, and drift standards were made from a 3000  $\mu\text{M}$  stock solution prepared by dissolving 0.5642  $\text{Na}_2\text{SiF}_6$  in 1000 mL of artificial seawater (NaCl solution with an ionic strength of 0.7). Calibration was achieved with the following standards: 30, 60, 120, 240, 360, 480, 600, 900, and 1200  $\mu\text{M}$   $\text{H}_4\text{SiO}_4$ . Two check standards, which were prepared from the stock solution but were not part of the calibration curve, with concentrations of 300 and 500  $\mu\text{M}$  were analyzed during each batch of analyses to monitor analytical accuracy. A 480  $\mu\text{M}$  drift standard was analyzed every 5 samples to monitor analytical precision. The average precision of the dissolved silica analyses based on repeated measurement of the 480, 300, and 500  $\mu\text{M}$  standards over a 1 month period was <1%, and the average accuracy based on repeated analysis of the 300 and 500  $\mu\text{M}$  check standards was <1.5%.

## Results and discussion

A total of 241 pore fluid samples were analyzed and the data are listed in Tables T1, T2, and T3.

Downhole distributions of Sr, B, Li, Mn, Ba, and  $\text{H}_4\text{SiO}_4$  at Sites U1378 and U1379 are shown in Figures F2 and F3. The most striking signature within the slope sediment apron cored at these sites is a concomitant increase in Ba, Sr, and  $\text{H}_4\text{SiO}_4$ , which at Site U1379 occurs from ~300 to 450 mbsf, with maximum values of 7400 nM, 103  $\mu\text{M}$ , and 435  $\mu\text{M}$ , respectively. At Site U1378, there is a distinct maximum in Ba and  $\text{H}_4\text{SiO}_4$  between 10 and 30 mbsf, with Ba ranging from 1067 to 1667 nM and  $\text{H}_4\text{SiO}_4$  ranging from 560 to 700  $\mu\text{M}$ ; however, Sr decreases within these shal-

low sediments. In the sediment interval from ~200 to 400 mbsf, there are additional broad maxima in Ba (maximum = 7500 nM) and  $\text{H}_4\text{SiO}_4$  (maximum = 740  $\mu\text{M}$ ) and a slight but distinct Sr maxima (maximum = 56  $\mu\text{M}$ ). Whereas this preliminary data set is not enough to fully constrain the reactions leading to these concentration changes, it is likely that the maxima in Ba and  $\text{H}_4\text{SiO}_4$  are associated with alteration of reactive volcanic ash layers and dissolution of biogenic opal, and the Sr concentration reflects both ash alteration and carbonate diagenesis. At Site U1379 only two tephra layers are recognized in the uppermost 324 m of sediment, whereas 29 tephra layers were recognized between 309 and 500 mbsf, which correspond to the broad concentration maxima in Ba, Sr, and  $\text{H}_4\text{SiO}_4$ . Intense ash alteration within this interval is confirmed by a marked decrease in the  $^{87}\text{Sr}/^{86}\text{Sr}$  ratios measured in pore fluids (Ross et al., submitted). Tephra layers at Site U1378 are more widely distributed (Fig. F2). In Unit I, shipboard sedimentologists identified 21 tephra layers, widely distributed within the background silty clay sediment. Alteration of these silicates releases  $\text{H}_4\text{SiO}_4$ , Ba, and Sr to the pore fluids. From the 49 tephra horizons described in Unit II, 38 occur between 205 and 333 mbsf, which is also consistent with the pore water profiles. A decrease in strontium isotope values occurs at Site U1378, but the isotopic distribution at Site U1378 is less congruent with Sr concentration data, possibly due to more carbonate diagenesis at this site (Ross et al., submitted).

Li and B profiles reported from the Costa Rica margin offshore Nicoya (Chan and Kastner, 2000; Kopf et al., 2000) and convergent margins elsewhere (Moriguti and Nakamura, 1998, Teichert et al., 2005) have shown these elements to be modified in response to moderate to high temperatures. Li is released from solid phases at high temperatures, whereas B concentration in fluids have been shown to decrease as alteration proceeds. Li concentrations measured in samples from Sites U1378 and U1379 are lower than seawater values (26  $\mu\text{M}$ ) and are relatively constant in the upper 200 mbsf. Deeper than 200 mbsf, there is an increase in concentration with depth, which at Site U1379 leads to a maximum of 74  $\mu\text{M}$  at the bottom of the hole, suggesting diffusional interaction with fluid at a greater depth, where higher temperatures prevail. At Site U1378, Li concentrations increase rapidly to a maximum value of 59  $\mu\text{M}$  at 490 mbsf, followed by a slight decrease to the base of the hole. The zone of elevated Li concentrations at Sites U1378 and U1379 correlates with the broad shear zone observed above the unconformity between the slope apron and underlying wedge material. At Site U1378, this zone extends from ~480

to 550 mbsf and corresponds to a horizon with depleted Cl and Ca concentrations, suggesting that the shear zone supports migration of fluids that originated from a source depth where temperatures are  $>80^{\circ}\text{C}$  (see the “[Expedition 334 summary](#)” chapter [Expedition 334 Scientists, 2012a]; Torres et al., 2013). The decrease in Li concentrations below the shear zone at Site U1378 reflects the presence of a fluid at depth that has interacted with sediment and/or oceanic basement at a lower temperature. These inferences were confirmed by drilling deeper at this location during Expedition 344 (Harris, Sakaguchi, Petronotis, and the Expedition 344 Scientists, 2013; Torres et al., 2013).

Marine sediments constitute a major reservoir for boron (Ishikawa and Nakamura, 1993), an element that is a highly mobile and is involved in various diagenetic processes. An increase in concentration over the seawater value of  $450\ \mu\text{M}$  has been observed at various margin settings, and has been attributed to microbial alteration of organic matter, ammonium exchange reactions, and release from clays at higher temperatures (You et al., 1993, 1995). Although small, the shallow slope sediments cored at Site U1379 show slight enrichments in dissolved B (to  $472\ \mu\text{M}$ ), and a more developed enrichment is apparent in shallow sediments from Site U1378, with values ranging from  $493$  to  $594\ \mu\text{M}$  in the upper 30 mbsf. Below these shallow maxima, B concentrations decrease with depth to values as low as  $180$  and  $100\ \mu\text{M}$  at Sites U1378 and U1379, respectively. Detrital clay minerals initially adsorb B onto the mineral surface, and with increasing burial during late diagenesis, this element is incorporated in tetrahedral sites of the clay structure, replacing Si (Williams et al., 2001). However, B is released during smectite to illite conversion, as documented experimentally and in field observations (Williams et al., 2001; Teichert et al., 2005; You et al., 1995). The lack of an increase in B concentrations with depth at these CRISP slope sites suggests that the B released at depth is overprinted by sorption and incorporation onto clays; a very slight concentration increase at the shear zones may be indicative of a component of clay dehydration reactions, evidenced in the low Cl values measured in pore fluids from the shear zone (see the “[Expedition 334 summary](#)” chapter [Expedition 334 Scientists, 2012a]). However, full evaluation of the processes driving B reactions in the CRISP region awaits results from boron isotopic analyses (Solomon laboratory, in progress).

Mn concentrations at Sites U1378 and U1379 are highly variable, and the discrete maxima in the re-

ducing fluids at these sites possibly indicate alteration of Mn-bearing tephtras.

Downhole distributions of Sr, B, Li, Mn, Ba, and  $\text{H}_4\text{SiO}_4$  at Site U1381 are shown in Figure [F4](#). Sr concentrations are close to a modern seawater value of  $86\ \mu\text{M}$  from the seafloor to  $\sim 45$  mbsf and increase slightly downhole from  $\sim 45$  to  $\sim 95$  mbsf to a maximum concentration of  $104\ \mu\text{M}$ . In the deepest  $\sim 10$  m of the hole, Sr concentrations decrease slightly toward the sediment/basalt interface. The minor decrease in Sr concentrations observed at the base of the hole must be related to reactions in the oceanic basement, as confirmed by strontium isotope data (Ross et al., submitted).

In the shallowest sample analyzed at  $\sim 1.5$  mbsf,  $\text{H}_4\text{SiO}_4$  concentration ( $538\ \mu\text{M}$ ) is higher than bottom water concentration, which in this region is  $\sim 180\ \mu\text{M}$ . Silica concentrations increase with depth to  $\sim 1080\ \mu\text{M}$ , possibly in response to the dissolution of siliceous phyto- and zooplankton diatoms, radiolarians, and sponge spicules observed in larger abundances in lithostratigraphic Unit II (see the “[Expedition 334 summary](#)” chapter [Expedition 334 Scientists, 2012a]).

Ba concentrations throughout the sediment section are very low, between  $\sim 250$  and  $730\ \text{nM}$ , and slightly above the bottom seawater concentration of  $\sim 240$ – $470\ \text{nM}$ . These concentrations are typical of pore fluid Ba values in the pelagic environment, where sulfate concentrations are too high for barite dissolution. No obvious trends are observed in the Ba concentration-depth profile, as expected for this environment. From  $\sim 25$  mbsf to the bottom of the hole, Mn concentrations increase with depth, similar to the Li profile. This Mn increase has a diffusional shape, suggesting communication with deeper fluid in the oceanic basement that has a higher Mn concentration. As observed in the shallow sediments cored in the slope apron, B shows a slight increase over seawater values to  $554\ \mu\text{M}$ , with a general decrease toward seawater values at the bottom of the hole.

## Acknowledgments

This research used samples and data provided by the Integrated Ocean Drilling Program (IODP), which is sponsored by the US National Science Foundation and participating countries and universities under management of IODP Management International, Inc. The outstanding efforts of the Siem Offshore officers and crew as well as the drilling personnel and

the scientific parties of IODP Expedition 344 are greatly acknowledged here. Without their hard work and dedication, none of these samples could have been recovered for analysis. This research was funded by USSP postcruise research Award T334B11 to M. Torres and Award T334A85 to E. Solomon.

## References

- Chan, L.-H., and Kastner, M., 2000. Lithium isotopic compositions of pore fluids and sediments in the Costa Rica subduction zone: implications for fluid processes and sediment contribution to the arc volcanoes. *Earth Planet. Sci. Lett.*, 183(1–2):275–290. doi:10.1016/S0012-821X(00)00275-2
- Expedition 334 Scientists, 2012a. Expedition 334 summary. In Vannucchi, P., Ujiie, K., Stroncik, N., Malinverno, A., and the Expedition 334 Scientists, *Proc. IODP, 334*: Tokyo (Integrated Ocean Drilling Program Management International, Inc.). doi:10.2204/iodp.proc.334.101.2012
- Expedition 334 Scientists, 2012b. Methods. In Vannucchi, P., Ujiie, K., Stroncik, N., Malinverno, A., and the Expedition 334 Scientists, *Proc. IODP, 334*: Tokyo (Integrated Ocean Drilling Program Management International, Inc.). doi:10.2204/iodp.proc.334.102.2012
- Expedition 334 Scientists, 2012c. Site U1378. In Vannucchi, P., Ujiie, K., Stroncik, N., Malinverno, A., and the Expedition 334 Scientists, *Proc. IODP, 334*: Tokyo (Integrated Ocean Drilling Program Management International, Inc.). doi:10.2204/iodp.proc.334.103.2012
- Expedition 334 Scientists, 2012d. Site U1379. In Vannucchi, P., Ujiie, K., Stroncik, N., Malinverno, A., and the Expedition 334 Scientists, *Proc. IODP, 334*: Tokyo (Integrated Ocean Drilling Program Management International, Inc.). doi:10.2204/iodp.proc.334.104.2012
- Expedition 334 Scientists, 2012e. Site U1381. In Vannucchi, P., Ujiie, K., Stroncik, N., Malinverno, A., and the Expedition 334 Scientists, *Proc. IODP, 334*: Tokyo (Integrated Ocean Drilling Program Management International, Inc.). doi:10.2204/iodp.proc.334.106.2012
- Gieskes, J.M., Gamo, T., and Brumsack, H., 1991. Chemical methods for interstitial water analysis aboard JOIDES Resolution. *ODP Tech. Note*, 15. doi:10.2973/odp.tn.15.1991
- Harris, R.N., Sakaguchi, A., Petronotis, K., and the Expedition 344 Scientists, 2013. *Proc. IODP, 344*: College Station, TX (Integrated Ocean Drilling Program). doi:10.2204/iodp.proc.344.2013
- Ishikawa, T., and Nakamura, E., 1993. Boron isotope systematics of marine sediments. *Earth Planet. Sci. Lett.*, 117(3–4):567–580. doi:10.1016/0012-821X(93)90103-G
- Kopf, A., Deyhle, A., and Zuleger, E., 2000. Evidence for deep fluid circulation and gas hydrate dissociation using boron and boron isotopes of pore fluids in forearc sediments from Costa Rica (ODP Leg 170). *Mar. Geol.*, 167(1–2):1–28. doi:10.1016/S0025-3227(00)00026-8
- LaFemina, P., Dixon, T.H., Govers, R., Norabuena, E., Turner, H., Saballos, A., Mattioli, G., Protti, M., and Strauch, W., 2009. Fore-arc motion and Cocos Ridge collision in Central America. *Geochem., Geophys., Geosyst.*, 10(5):Q05S14. doi:10.1029/2008GC002181
- Manheim, F.T., and Sayles, F.L., 1974. Composition and origin of interstitial waters of marine sediments, based on deep sea drill cores. In Goldberg, E.D. (Ed.), *The Sea* (Vol. 5): *Marine Chemistry: The Sedimentary Cycle*. New York (Wiley), 527–568.
- Moriguti, T., and Nakamura, E., 1998. Across-arc variation of Li isotopes in lavas and implications for crust/mantle recycling at subduction zones. *Earth Planet. Sci. Lett.*, 163(1–4):167–174. doi:10.1016/S0012-821X(98)00184-8
- Ranero, C.R., and von Huene, R., 2000. Subduction erosion along the Middle America convergent margin. *Nature*, 404(6779):748–752. doi:10.1038/35008046
- Ranero, C.R., von Huene, R., Flueh, E., Duarte, M., Baca, D., and McIntosh, K., 2000. A cross section of the convergent Pacific margin of Nicaragua. *Tectonics*, 19(2):335–357. doi:10.1029/1999TC900045
- Ross, N., Torres, M.E., Haley, B.A., Solomon, E., and Kastner, M., submitted. Data report: strontium isotope analyses of pore fluids from the CRISP-A transect drilled during Expeditions 334 and 344. *Proc. IODP, 344*.
- Teichert, B.M.A., Torres, M.E., Bohrmann, G., and Eisenhauer, A., 2005. Fluid sources, fluid pathways and diagenetic reactions across an accretionary prism revealed by Sr and B geochemistry. *Earth Planet. Sci. Lett.*, 239(1–2):106–121. doi:10.1016/j.epsl.2005.08.002
- Torres, M.E., Solomon, E.A., Kastner, M., Harris, R.N., Formolo, M., Choi, J., Berg, R.D., and Nuzzo, M., 2013. Geochemical evidence for fluid flow in the upper and subducting plates of the Costa Rica margin: results from CRISP drilling during Exp. 334 and 344 [presented at the 2013 American Geophysical Union Fall Meeting, San Francisco, CA, 9–13 December 2013]. (Abstract T34C-02) <http://abstractsearch.agu.org/meetings/2013/FM/sections/T/sessions/T34C/abstracts/T34C-02.html>
- Vannucchi, P., Galeotti, S., Clift, P.D., Ranero, C.R., and von Huene, R., 2004. Long-term subduction-erosion along the Guatemalan margin of the Middle America Trench. *Geology*, 32(7):617–620. doi:10.1130/G20422.1
- Vannucchi, P., Ujiie, K., Stroncik, N., Malinverno, A., and the Expedition 334 Scientists, 2012. *Proc. IODP, 334*: Tokyo (Integrated Ocean Drilling Program Management International, Inc.). doi:10.2204/iodp.proc.334.2012
- Williams, L.B., Hervig, R.L., Holloway, J.R., and Hutcheon, I., 2001. Boron isotope geochemistry during diagenesis. Part I. Experimental determination of fractionation during illitization of smectite. *Geochim. Cosmochim. Acta*, 65(11):1769–1782. doi:10.1016/S0016-7037(01)00557-9
- You, C.-F., Spivack, A.J., Gieskes, J.M., Rosenbauer, R., and Bischoff, J.L., 1995. Experimental study of boron geochemistry: implications for fluid processes in subduc-

tion zones. *Geochim. Cosmochim. Acta*, 59(12):2435–2442. doi:10.1016/0016-7037(95)00137-9

You, C.-F., Spivack, A.J., Smith, J.H., and Gieskes, J.M., 1993. Mobilization of boron in convergent margins: implications for the boron geochemical cycle. *Geology*, 21(3):207–210. doi:10.1130/0091-7613(1993)021<0207:MOBICM>2.3.CO;2

**Initial receipt:** 14 April 2014  
**Acceptance:** 23 July 2014  
**Publication:** 10 October 2014  
**MS 334-201**

**Figure F1.** A. Location map of the sites drilled during IODP Costa Rica Seismogenesis Project (CRISP). B. Location of Sites U1378, U1379, and U1381 on bathymetry. C. Location of sites on depth-migrated seismic Line BGR99-7. From the “[Expedition 334 summary](#)” chapter [Expedition 334 Scientists, 2012a].

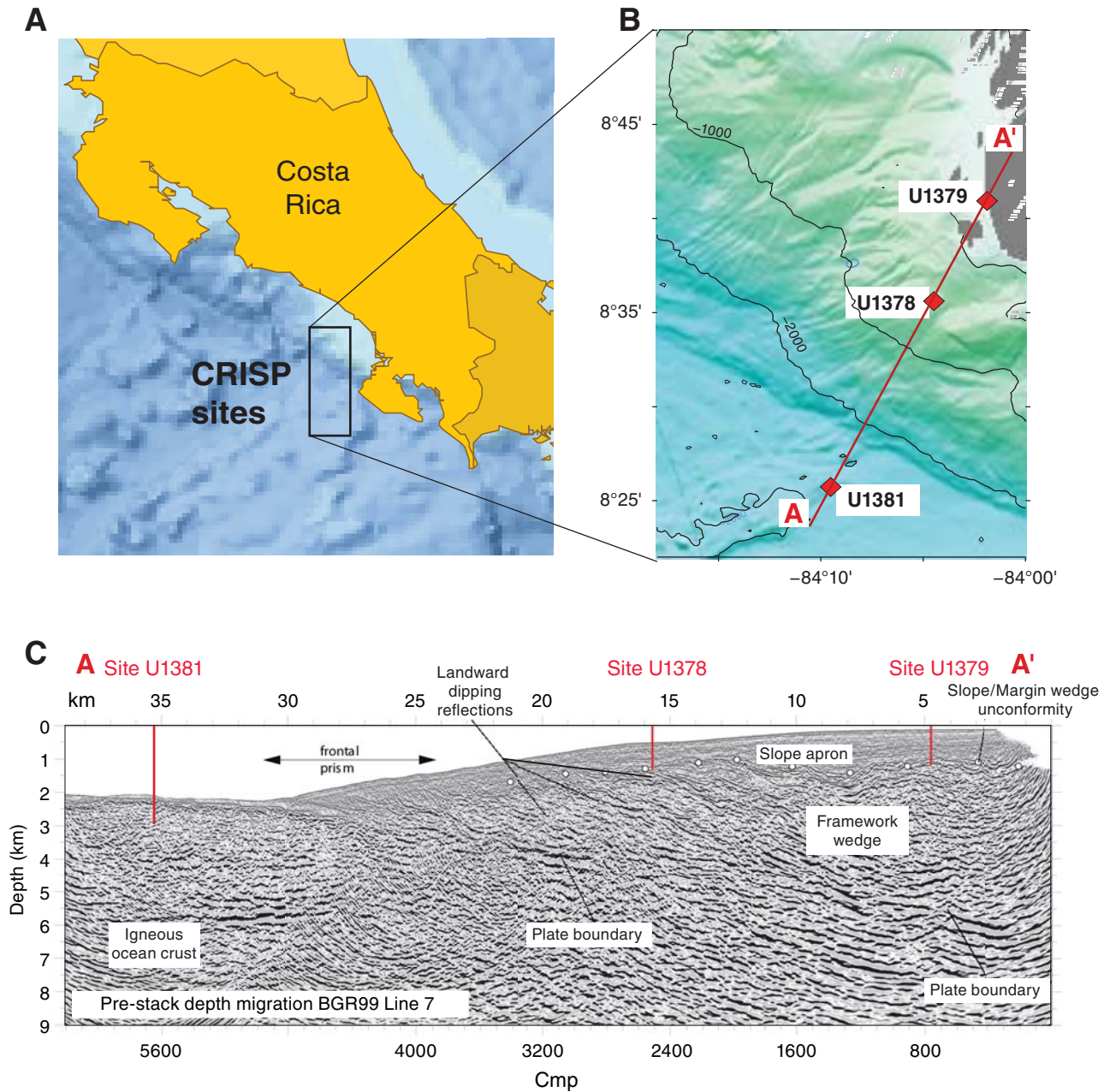


**Figure F2.** Downhole profiles of strontium, barium, silica, lithium, boron, and manganese, Site U1378. Lithostratigraphic column is redrawn from the “[Site U1378](#)” chapter (Expedition 334 Scientists, 2012c). Arrows = bottom seawater values, dashed line = lithostratigraphic unit boundary.

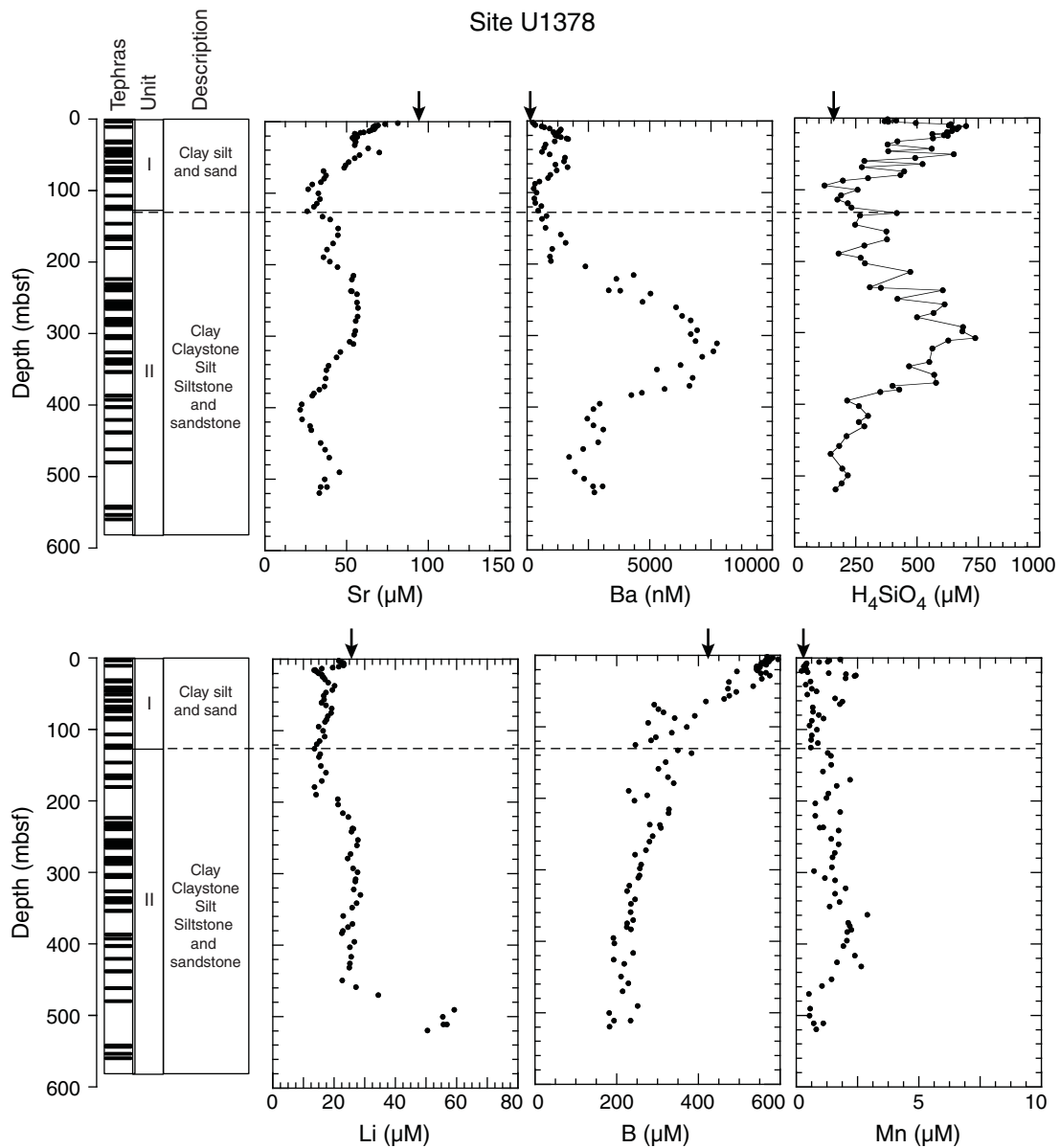


**Figure F3.** Downhole profiles of strontium, barium, silica, lithium, boron, and manganese, Site U1379. Lithostratigraphic column is redrawn from the “Site U1379” chapter (Expedition 334 Scientists, 2012d). Arrows = bottom seawater values., dashed lines = lithostratigraphic unit boundaries.

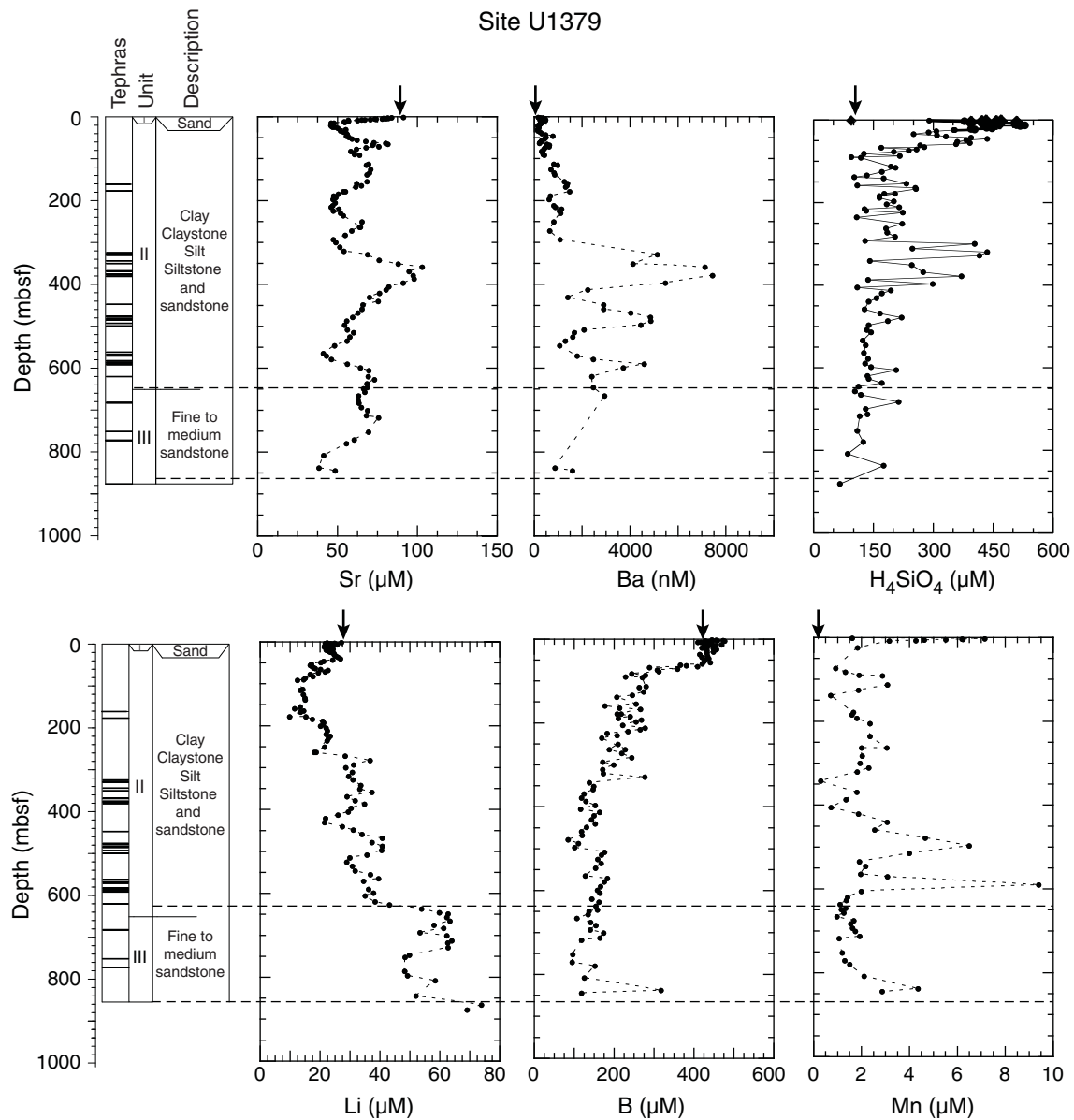


**Figure F4.** Downhole profiles of strontium, barium, silica, lithium, boron, and manganese, Site U1381. Lithostratigraphic column is redrawn from the “Site U1381” chapter (Expedition 334 Scientists, 2012e). Arrows = bottom seawater values, dashed line = lithostratigraphic unit boundary.

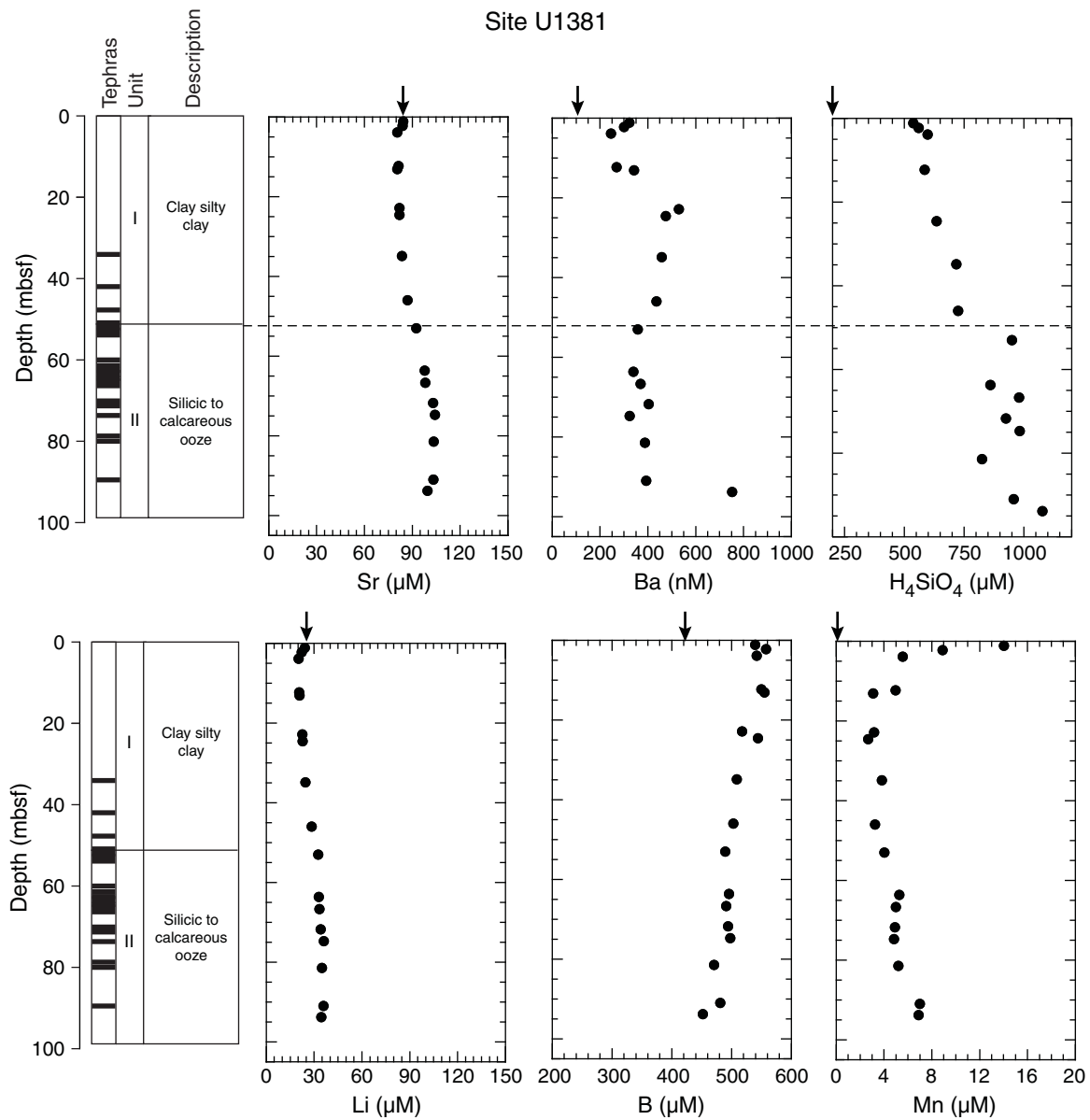


Table T1. Minor element concentrations in pore fluids, Site U1378. (Continued on next page.)

Core, section, interval (cm)	Depth (mbsf)		Li ( $\mu\text{M}$ )	B ( $\mu\text{M}$ )	Mn ( $\mu\text{M}$ )	Sr ( $\mu\text{M}$ )	Ba (nM)	$\text{H}_4\text{SiO}_4$ ( $\mu\text{M}$ )
	Top	Bottom						
334-U1378B-								
1H-1, 138-150	1.4	1.5	21.3	567	1.78	81.1	252	381
1H-2, 138-150	2.9	3.0	21.9	581	1.33	73.2	269	414
1H-3, 138-150	4.4	4.5	22.7	577	1.27	69.0	329	370
1H-4, 46-58	5.0	5.1	22.9	594	0.92	67.3	325	384
2H-1, 138-150	6.7	6.8	23.1	562	0.41	66.0	604	496
2H-2, 138-150	8.2	8.3	22.9	571	0.37	67.2	703	637
2H-3, 138-150	9.7	9.8	21.4	553	0.37	66.5	912	631
2H-4, 138-150	11.2	11.3	19.4	558	0.29	64.9	1357	700
2H-5, 138-150	12.7	12.8	15.8	565	0.31	63.5	1349	670
2H-6, 138-150	14.2	14.3	13.6	547	0.31	60.2	1320	649
2H-7, 54-66	14.8	15.0	13.4	542	0.38	58.2	1067	663
3H-1, 138-150	16.2	16.3	14.0	549	0.32	54.8	1132	646
3H-2, 138-150	17.7	17.8	14.4	541	0.19	55.7	1179	643
3H-3, 138-150	19.2	19.3	14.8	541	0.45	55.0	1157	624
3H-4, 138-150	20.7	20.8	15.7	544	1.31	56.2	1243	626
3H-5, 138-150	22.2	22.3	15.9	493	2.01	53.3	1363	562
3H-6, 133-145	23.6	23.8	16.1	564	2.41	54.8	1609	612
3H-7, 58-70	24.4	24.5	16.4	552	2.36	54.6	1667	627
4H-3, 138-150	27.8	27.9	16.9	574	1.99	55.3	1143	566
4H-6, 138-150	32.3	32.4	17.9	554	0.57	54.6	753	421
5H-2, 138-150	36.7	36.8	20.0	473	0.37	63.0	727	380
5H-6, 138-150	42.7	42.8	19.3	533	0.62	69.8	611	561
6H-2, 138-150	46.2	46.3	17.2	471	0.81	57.7	943	382
6H-5, 138-150	50.7	50.8	16.5	492	0.43	54.8	1546	650
7H-2, 138-150	55.7	55.8	16.5	474	1.56	51.1	1518	494
7H-5, 138-150	60.2	60.3	15.8	461	1.86	49.0	1145	285
8H-2, 138-150	63.8	63.9	17.2	417	1.75	48.2	1630	524
8H-5, 138-150	68.3	68.4	19.0	291	0.65	35.5	1202	276
9H-2, 138-150	74.7	74.8	18.8	301	0.67	37.1	977	448
9H-5, 130-142	79.1	79.2	17.9	314	0.90	36.0	858	433
10H-2, 130-142	84.1	84.2	17.5	390	1.09	34.1	511	301
10H-4, 138-150	87.1	87.2	16.9	341	0.61	28.7	310	198
11H-3, 138-150	94.0	94.1	14.8	276	0.52	26.1	286	124
12H-3, 138-150	99.8	100.0	16.2	371	0.83	32.4	395	258
13H-4, 138-150	107.9	108.0	16.8	334	0.62	33.4	312	190
14H-3, 138-150	114.1	114.2	15.1	295	0.59	31.5	330	176
15H-2, 118-130	118.5	118.6	14.2	283	0.87	29.7	597	218
16H-3, 133-145	124.8	124.9	13.4	245	0.58	25.7	452	233
17X-3, 133-145	132.1	132.3	15.3	348	1.27	35.0	783	418
18X-3, 113-130	136.3	136.5	14.9	382	1.40	39.8	629	267
19X-5, 71-96	148.6	148.8	15.5	319	1.41	44.6	759	249
20X-5, 130-153	158.2	158.5	17.2	301	1.08	44.4	1356	375
21X-7, 68-93	169.6	169.9	15.8	325	2.18	41.5	1553	378
22X-5, 88-105	178.2	178.4	13.4	338	1.63	37.7	1007	285
23X-6, 109-126	188.8	189.0	14.0	228	1.30	35.6	922	182
24X-4, 122-150	194.9	195.2	21.0	273	1.21	39.5	966	271
25X-3, 74-90	202.7	202.9	21.2	242	0.75	44.2	2324	289
26X-4, 98-115	214.7	214.9	22.7	327	1.77	53.9	4274	474
27X-2, 100-127	220.0	220.3	24.5	326	0.76	52.9	3549	
28X-7, 33-65	236.4	236.8	25.8	280	1.08	52.4	3233	308
29X-3, 45-83	236.8	237.1	26.2	305	0.94	52.9	3725	353
30X-2, 110-145	240.9	241.3	25.6	307	1.71	56.2	4958	607
31X-4, 118-150	252.5	252.8	27.6	286	1.41	56.1	4593	420
32X-3, 73-105	259.8	260.2	27.3	279	1.71	56.7	5866	614
33X-5, 58-94	271.9	272.3	25.2	270	1.55	56.4	6189	568
34X-2, 86-122	278.0	278.3	24.3	244	1.46	55.4	6506	502
35X-5, 98-130	292.1	292.4	26.0	259	1.43	55.1	6767	687
36X-2, 93-125	297.6	298.0	27.5	256	0.70	54.4	6482	685
37X-2, 91-123	307.2	307.5	26.9	255	1.15	51.5	6692	739
38X-1, 118-150	310.5	310.8	26.8	252	1.56	53.9	7494	629
39X-5, 118-150	321.7	322.0	26.3	230	1.99	46.0	7361	564
40X-4, 80-92	329.1	329.2	28.5	224	1.56	43.6	6901	
41X-5, 104-136	340.7	341.1	27.2	244	1.74	38.7	6015	551
42X-3, 64-96	347.0	347.4	25.8	234	1.34	37.4	5145	467
43X-5, 55-87	358.7	359.0	22.9	233	2.87	36.9	6469	571
45X-3, 55-88	369.7	370.0	25.9	240	2.10	36.1	6333	578
46X-2, 115-150	374.3	374.6	24.4	224	2.16	33.1	5393	401

Table T1 (continued).

Core, section, interval (cm)	Depth (mbsf)		Li ( $\mu\text{M}$ )	B ( $\mu\text{M}$ )	Mn ( $\mu\text{M}$ )	Sr ( $\mu\text{M}$ )	Ba (nM)	$\text{H}_4\text{SiO}_4$ ( $\mu\text{M}$ )
	Top	Bottom						
47X-2, 95–130	379.4	379.7	22.7	224	2.23	29.8	4515	429
48X-1, 96–122	382.9	383.1	22.4	233	2.06	28.7	4070	351
49X-3, 106–138	394.7	395.0	26.5	191	2.05	22.2	2834	215
50X-2, 97–129	402.3	402.6	25.0	193	1.90	21.3	2588	262
51X-5, 85–117	416.0	416.3	25.5	239	2.38	22.5	2352	301
52X-5, 70–102	425.0	425.3	25.0	192	1.64	27.3	2570	264
53X-3, 53–85	430.7	431.0	24.7	217	2.63	28.1	2959	285
54X-5, 104–140	444.2	444.6						212
55X-2, 81–117	448.8	449.2	22.5	210	1.42	33.9	2797	
56X-2, 64–76	458.2	458.4	27.0	228	1.03	36.5	2197	184
57X-3, 63–99	469.3	469.7	34.3	214	0.49	39.1	1670	148
58X-2, 90–126	478.3	478.6						
59X-4, 93–125	489.7	490.0	59.1	250	0.55	45.3	1909	196
60X-4, 60–92	499.7	500.0	55.3	181	0.52	36.4	2247	219
61X-4, 102–138	510.1	510.5	56.6	192	0.69	33.8	2561	194
62X-1, 54–81	510.2	510.5	55.5	233	1.08	37.7	2979	
63X-4, 84–122	518.7	519.1	50.3	181	0.79	33.0	2622	169
Limit of detection:			0.82	4.3	0.19	0.67	84	

Table T2. Minor element concentrations in pore fluids, Site U1379. (Continued on next two pages.)

Core, section, interval (cm)	Depth (mbsf)		Li ( $\mu\text{M}$ )	B ( $\mu\text{M}$ )	Mn ( $\mu\text{M}$ )	Sr ( $\mu\text{M}$ )	Ba (nM)	$\text{H}_4\text{SiO}_4$ ( $\mu\text{M}$ )
	Top	Bottom						
334-U1379B-								
1H-1, 70–80	0.7	0.8	27.0	444	1.59	91.1	157	95
2H-1, 110–120	2.1	2.2	24.7	472	7.13	81.0	369	433
2H-2, 35–45	2.9	3.0	23.4	458	6.18	78.5	342	470
2H-2, 110–120	3.6	3.7	24.6	476	6.21	80.1	408	422
2H-3, 35–45	4.4	4.5	22.6	444	5.49	73.0	361	458
2H-3, 110–120	5.1	5.2	22.2	409	4.60	73.8	383	395
2H-4, 35–35	5.9	6.0						509
2H-4, 110–120	6.6	6.7	21.6	433	4.24	64.8	391	466
2H-5, 88–98	7.9	8.0	24.0	404	3.14	56.6	268	458
334-U1379C-								
1H-1, 140–150	1.4	1.5	25.5	454		83.6	334	290
1H-2, 140–150	2.9	3.0	23.5	428		81.7	418	378
1H-3, 140–150	4.4	4.5	22.8	435		77.7	457	427
1H-4, 140–150	5.9	6.0	21.3	425		70.4	534	431
1H-5, 50–60	6.5	6.6	21.3	417		66.8	553	468
2H-1, 140–150	8.1	8.2	21.7	427		62.4	549	515
2H-2, 140–150	9.6	9.7	22.9	423		56.8	430	504
2H-3, 140–150	11.1	11.2	23.6	438		53.9	349	508
2H-4, 140–150	12.6	12.7	24.2	468		54.3	430	530
2H-5, 140–150	14.1	14.2	21.9	446		47.5	382	518
2H-6, 36–46	14.6	14.7	22.4	453		45.8	373	436
3H-1, 138–148	17.6	17.7	23.0	429		46.6	307	433
3H-2, 138–148	19.1	19.2	23.4	432		46.6	287	447
3H-3, 138–148	20.6	20.7	23.8	419		45.6	229	396
3H-4, 138–148	22.1	22.2	24.6	448		46.2	240	404
3H-5, 138–148	23.6	23.7	24.6	428		46.7	268	354
3H-6, 39–39	24.1	24.2	25.2	444	1.72	47.2	133	352
4H-2, 138–148	27.1	27.2	25.9	431		50.0	256	307
4H-4, 92–102	29.6	29.7	26.7	448		54.9	220	289
5H-2, 138–148	33.1	33.2	24.1	431		51.7	231	251
5H-4, 149–159	36.2	36.3	21.1	414		53.6	327	309
6H-2, 138–148	39.4	39.5	20.1	433		55.5	392	332
6H-4, 138–148	42.4	42.5	17.1	419		55.9	551	396
7H-2, 138–148	45.4	45.5	16.6	436		55.3	852	435
7H-4, 136–146	48.4	48.5	17.2	427		56.8	569	383
8H-2, 138–148	52.0	52.1	17.8	424		58.9	504	360
8H-4, 130–140	54.9	55.0	18.3	440		61.8	393	391
9H-2, 138–148	58.4	58.5	20.0	420		67.5	360	358
9H-4, 128–138	61.3	61.4	22.5	365		72.5	304	267
10H-1, 88–98	62.4	62.5	21.6	380		79.8	298	
11H-1, 138–148	64.9	65.0	19.3	408		81.2	608	278
11H-3, 78–88	67.3	67.4	16.5	288		71.7	712	171

Table T2 (continued). (Continued on next page.)

Core, section, interval (cm)	Depth (mbsf)		Li ( $\mu\text{M}$ )	B ( $\mu\text{M}$ )	Mn ( $\mu\text{M}$ )	Sr ( $\mu\text{M}$ )	Ba (nM)	H <sub>4</sub> SiO <sub>4</sub> ( $\mu\text{M}$ )
	Top	Bottom						
12H-2, 138–148	70.6	70.7	17.6	358		75.6	698	258
12H-4, 103–103	73.2	73.3	15.6	311	0.94	65.5	433	239
13H-2, 138–148	76.6	76.7	14.4	311		61.5	478	202
14H-2, 138–138	81.6	81.7	12.3	232	1.22	56.2	239	127
15H-3, 100–110	86.2	86.3	14.1	278		59.9	433	216
16H-2, 138–138	89.4	89.5	13.5	222	1.86	58.8	340	95
17H-1, 76–76	91.0	91.1	14.4	263	2.80	61.8	395	118
20X-1, 137–137	112.1	112.2	14.8	273	2.99	66.8	790	193
20X-3, 137–147	115.1	115.2	14.9	262		67.9	1051	206
21X-3, 133–133	124.8	124.9	13.9	268	1.87	68.6	670	171
22X-3, 137–137	133.5	133.6	13.3	244		69.8	908	134
22X-6, 138–138	138.0	138.1	11.6	205	0.87	66.4	847	102
23X-1, 138–148			14.4	253		68.7	944	176
23X-6, 113–123			13.8	197		68.5	1136	
24X-3, 133–148	154.2	154.4	13.3	254		68.2	1329	233
24X-6, 124–139	158.6	158.8	9.7	176		61.8	1461	110
25X-3, 133–148	164.0	164.2	15.1	212		64.7	1445	255
25X-5, 128–143	167.0	167.2	17.3	265		61.2	1388	256
26X-3, 133–148	178.1	178.3	20.7	206		54.7	1554	178
26X-6, 113–130	178.1	178.3	22.0	216	1.47	52.8	1360	204
27X-3, 133–150	183.6	183.8	21.3	239	1.51	49.0	852	165
27X-6, 113–130	187.9	188.1	20.1	209		47.3	751	166
28X-3, 133–133	192.3	192.4	22.2	265	1.71	47.6	595	
28X-6, 133–143	196.7	196.8	22.4	254		47.0	696	202
29X-1, 133–150	200.2	200.4						
29X-4, 120–137	204.5	204.7	22.5	220	2.32	45.4	737	183
30X-2, 133–143	211.5	211.6	23.2	277		46.7	892	215
30X-5, 123–133	215.4	215.5	22.6	264		45.7	965	128
31X-2, 133–148	219.3	219.5	22.2	234		50.6	1213	133
31X-5, 133–148	223.8	224.0	18.5	182		47.1	1125	224
32X-2, 133–148	229.1	229.3	21.4	206		51.5	1178	
32X-6, 133–133	235.1	235.3	18.6	172	2.31	52.3	707	108
33X-5, 78–100	262.5	262.7	29.9	229	2.89	62.4	737	
34X-3, 128–148	250.2	250.4	36.5	209		65.1	894	222
35X-5, 78–100	262.5	262.7	31.8	189	1.98	61.4	615	182
36X-5, 128–128	271.7	271.9	28.4	218		58.6	725	185
37X-5, 128–128	282.6	282.8	32.2	243	1.93	53.0	608	204
38X-5, 128–128	292.4	292.6	29.4	170		47.0	1158	129
39X-3, 129–129	299.2	299.4	31.0	199	1.87	47.0	1100	404
40X-4, 100–122	310.2	310.4	32.7	165	2.15	48.1	1566	249
41X-4, 128–128	320.3	320.5	34.0	167	1.79	51.4	1993	435
42X-3, 123–145	328.4	328.7	37.2	276		68.6	5226	416
43X-6, 81–107	341.4	341.7	29.4	144	<dl	72.6	2332	141
44X-6, 78–107	350.9	351.2	31.6	148		87.7	4203	246
45X-4, 118–140	358.4	358.6	34.7	146		102.8	7210	
46X-5, 75–100	368.5	368.7	30.8	125	1.87	91.5	7422	275
47X-5, 133–156	378.0	378.3						370
48X-6, 63–63	386.4	386.5	26.6	134	1.35	95.0	5701	137
49X-6, 75–100	395.9	396.1	21.7	152		90.9	5555	299
50X-5, 104–132	405.1	405.4	21.7	117	0.69	79.2	2816	110
51X-4, 104–129	412.5	412.8	27.3	163		80.1	2308	194
52X-2, 118–118	420.1	420.3	31.5	149	1.77	72.5	1676	171
53X-3, 118–118	430.4	430.6	33.9	143		69.7	1479	158
54X-4, 75–75	439.6	439.8	41.2	158	2.96	72.5	3201	138
55X-3, 87–87	448.1	448.3	37.2	130		65.6	2981	
56X-4, 100–100	458.7	458.9	41.3	115	2.47	62.4	2856	127
57X-3, 118–150	467.6	467.9	40.4	119		62.6	4109	166
58X-4, 90–90	477.5	477.8	36.3	82	4.52	56.5	4780	220
59X-4, 106–138	486.7	487.0	29.8	109		55.5	4947	186
60X-4, 118–150	496.4	496.7	29.8	99	6.46	52.0	4422	138
61X-5, 118–118	507.6	507.8	30.6	175		55.8	2154	134
62X-4, 68–100	514.5	514.8	32.0	164	3.90	57.1	1691	144
63X-5, 118–118	524.9	525.1	36.7	158		57.5	1686	
64X-5, 125–150	534.4	534.6	40.2	164	1.97	53.2	1320	123
65X-6, 78–114	545.1	545.4	35.0	152	2.16	45.0	1070	132
66X-6, 66–100	554.2	554.5						
67X-6, 70–70	563.8	564.1	37.1	132	1.83	39.0	1763	127
68X-4, 88–120	570.4	570.7	38.1	179	3.02	40.6	1775	
69X-3, 93–93	578.3	578.6	34.9	174		45.9	2549	137
70X-4, 92–92	589.7	590.0	39.3	164	9.28	54.1	4622	129

Table T2 (continued).

Core, section, interval (cm)	Depth (mbsf)		Li ( $\mu\text{M}$ )	B ( $\mu\text{M}$ )	Mn ( $\mu\text{M}$ )	Sr ( $\mu\text{M}$ )	Ba (nM)	$\text{H}_4\text{SiO}_4$ ( $\mu\text{M}$ )
	Top	Bottom						
71X-4, 64–64	598.5	598.8	43.1	157		64.0	3799	145
72X-2, 88–120	605.3	605.6	55.5	175	1.99	66.5	2521	208
73X-5, 116–150	619.6	619.9	60.6	141	1.36	65.7	2366	136
74X-4, 74–107	626.3	626.7	65.6	172	1.38	71.9	2943	138
75X-4, 86–120	636.4	636.7	65.0	159	1.20	66.9	2964	171
76X-3, 118–150	645.2	645.5	64.6	157	1.28	66.4	2462	113
77X-2, 118–150	648.5	648.8	59.8	138	1.16	64.0	2288	
78X-4, 110–150	656.6	657.0	63.6	143	1.18	64.8	2932	104
79X-4, 70–100	665.0	665.3	61.6	117	1.00	62.3	3186	119
80X-4, 93–125	674.7	675.1	63.4	141	1.62	58.6	3438	
81X-2, 100–132	682.0	682.3	67.4	155	1.53	61.4	3619	214
82X-3, 70–102	692.6	692.9	65.6	152	1.64	62.6	2511	
83X-1, 60–92	699.8	700.1	64.8	173	1.72	65.7	2012	131
84X-3, 56–88	712.4	712.7	53.0	167	1.65	67.0	1194	135
85X-1, 77–112	717.2	717.5	50.0	126	1.00	73.4	1396	116
86X-2, 87–119	728.5	728.8						
88X-1, 118–150	746.6	746.9						
89X-2, 0–40	751.6	752.0	48.8	103	1.14	66.1	1289	110
91X-4, 50–85	770.3	770.7	50.1	99	1.24	56.3	1161	
92X-3, 94–131	778.9	779.3	60.4	153	1.47	53.0	1034	125
93X-1, 22–50	785.2	785.5						
94X-1, 56–91	795.1	795.4						
95X-3, 118–150	807.5	807.8	54.1	135	2.15	39.4	840	86
97X-2, 68–100	824.8	825.1						
98X-4, 79–115	837.3	837.6	76.5	318	4.33	36.5	934	176
99X-2, 118–150	844.2	844.5	70.5	119	2.80	46.4	1641	
100X-2, 56–88	852.7	853.0						
101X-4, 58–90	865.3	865.6						
102X-5, 110–140	877.4	877.7						
103X-2, 34–60	881.2	881.5						66
Limit of detection:			2.4	6.4	0.28	1.1	70	

dl = detection limit.

Table T3. Minor element concentration in pore fluids, Site U1381.

Core, section, interval (cm)	Depth (mbsf)		Li ( $\mu\text{M}$ )	B ( $\mu\text{M}$ )	Mn ( $\mu\text{M}$ )	Sr ( $\mu\text{M}$ )	Ba (nM)	$\text{H}_4\text{SiO}_4$ ( $\mu\text{M}$ )
	Top	Bottom						
334-U1381A-								
3R-1, 61–71	13.0	13.1	20.4	554	3.05	80.2	362	644
4R-1, 46–56	22.8	22.9	22.5	517	3.12	81.7	554	656
5R-2, 135–150	34.8	34.9	24.2	508	3.78	83.2	497	719
6R-3, 135–150	45.9	46.0	27.9	502	3.22	86.8	479	726
7R-2, 60–75	52.9	53.0	30.9	489	4.00	92.3	378	951
8R-2, 135–150	63.6	63.7	33.0	495	5.25	97.4	367	860
8R-4, 135–150	66.6	66.7	33.2	490	4.95	97.9	385	980
9R-1, 135–150	71.7	71.8	34.1	493	4.89	102.8	427	925
9R-3, 135–150	74.7	74.8	35.0	497	4.80	104.0	335	984
10R-1, 145–158	81.4	81.5	34.2	470	5.17	103.1	384	826
11R-1, 135–150	90.9	91.0	34.7	480	6.95	103.0	381	959
11R-3, 120–135	93.7	93.9	34.1	451	6.85	99.2	730	1077
334-U1381B-								
1R-1, 100–115	1.0	1.2	23.8	539	14.00	84.1	333	538
1R-2, 100–115	2.2	2.3	22.0	557	8.86	83.6	293	560
1R-3, 150–165	3.8	4.0	19.9	541	5.53	80.4	256	599
2R-2, 130–150	12.2	12.4	20.2	549	4.91	81.0	293	586
3R-4, 100–120	24.5	24.7	22.5	543	2.64	81.7	523	637
Limit of detection:			2.4	6.4	0.28	1.1	70	